

Electrical Non-Hermitian Control of Topological Magnon Spin Transport

Pieter M. Gunnink,^{1,*} Rembert A. Duine,^{2,3} and Alexander Mook¹

¹*Institute of Physics, Johannes Gutenberg-University Mainz, Staudingerweg 7, Mainz 55128, Germany*

²*Institute for Theoretical Physics and Center for Extreme Matter and Emergent Phenomena, Utrecht University, Leuvenlaan 4, 3584 CE Utrecht, The Netherlands*

³*Department of Applied Physics, Eindhoven University of Technology, P.O. Box 513, 5600 MB Eindhoven, The Netherlands*

(Dated: January 11, 2024)

Magnonic topological phases realize chiral edge spin waves that are protected against backscattering, potentially enabling highly efficient spin transport. Here we show that the spin transport through these magnonic chiral edge states can be electrically manipulated by non-Hermitian control. We consider the paradigmatic magnon Haldane model and show that it is transformed into an effective non-Hermitian magnon Chern insulator by including a sublattice-dependent spin-orbit torque. In linear spin-wave theory, this electrically induced torque causes a lasing of the chiral edge magnons along certain edge directions, leading to an enhancement of the spin-wave amplitude. This prediction is confirmed by numerical simulations based on the Landau-Lifshitz-Gilbert equation. For a spin-wave transport setup, in which magnons are excited by a microwave field and detected with a normal metal conductor, we find that the magnon amplification is remarkably robust against disorder, establishing non-Hermitian control as a promising avenue for topological magnonics.

Introduction. Magnonics is a promising platform for the transport and manipulation of the spin degree of freedom, bypassing the Joule heating associated with conventional electronic devices [1]. To improve the efficiency of magnon spin transport, it has recently been proposed to exploit magnonic topological phases, where topological spin transport is possible. Various topological magnon phases have been proposed, such as magnon Chern insulators [2–9], magnon spin Hall insulators [10–12], magnon Dirac [13, 14] and Weyl [15, 16] systems. Of these, central to the field of magnon topology is the magnon Chern insulator, because its one-dimensional chiral edge modes are protected against backscattering, potentially enabling highly efficient spin transport [17, 18].

Magnonic systems naturally couple to their environment. For example, environmental couplings include (non-)local dissipation [19–23], non-reciprocal couplings [24, 25], and local pumping through a spin-transfer torque [26, 27]. These couplings are a curse and a blessing at the same time: although they provide additional functionality [28], they are also responsible for the finite lifetime of the magnons, which limits the propagation distances.

In this work, we show that the coupling to the environment can also be harnessed to increase the lifetime of magnons. In particular, we find that the lifetime of the edge modes is selectively enhanced. This way, one gains electrical control over the topological spin transport, allowing for the amplification of the chiral edge modes. Concretely, we consider a magnon Chern insulator coupled to a metallic layer in such a way that sublattice-dependent spin-orbit torques modulate the spin dynamics, and identify a protocol to make the topological edge modes lasing. We demonstrate this effect in Fig. 1, where an edge magnon is launched and detected after it has passed around the sample. Depending on which edge it travels through, the magnon is amplified, unaffected, or suppressed.

Furthermore, we study the magnon amplification in disordered systems, showing that the topological protection of the edge states remains, thus allowing for long-distance amplifi-

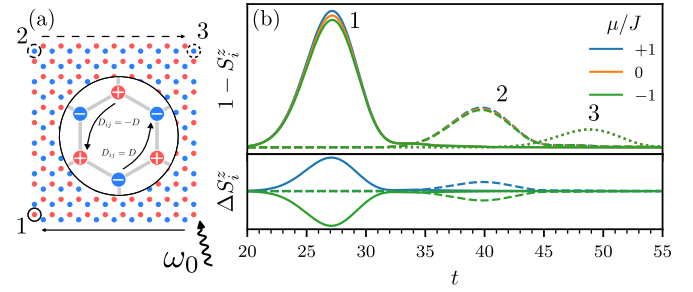


FIG. 1. Electrical control of a topological edge magnon, which is amplified after being excited with a pulse at frequency ω_0 at the bottom right corner of a rectangle shown in (a). The amplification is controlled by the sign of the applied spin bias μ . The spin-wave amplitude, $1 - S_i^z$, is shown in (b), for the three sites (1, 2, 3) indicated in (a). The difference $\Delta S_i^z \equiv S_i^z - S_i^z|_{\mu=0}$ is shown below, i.e., the difference as the spin bias is turned on. For $\mu > 0$, the zigzag edge indicated by a solid/dashed arrow amplifies/suppresses. The arm-chair edges do not amplify nor suppress. The inset to (a) shows the Haldane model used, including a positive ($\mu_i/J = +1$) and negative ($\mu_i/J = -1$) spin-orbit torque on the \mathcal{A} - and \mathcal{B} -sites respectively.

cation of spin transport. This is in contrast to previous approaches to modulate magnon spin transport [29–31], where the spin transport is not topologically protected. In addition, we show that our setup realizes a non-Hermitian topological phase, making the connection to the wider field of non-Hermitian topology [32–34] and topological insulator lasers in particular [35, 36], for which magnonic systems offer an promising platform [37–44]. We believe that our findings open a pathway to further on-chip manipulation of spin waves, offering an efficient scheme for the direct electrical control of propagating spin waves.

Model. We consider the magnon Haldane model, a prototypical model of the magnon Chern insulator [7, 8], with the inclusion of a sublattice-dependent spin-orbit torque, as shown in Fig. 1(a). The spin dynamics are described by the

Landau-Lifshitz-Gilbert equation,

$$\partial_t \mathbf{S}_i = \mathbf{S}_i \times \left(-\frac{\partial \mathcal{H}}{\partial \mathbf{S}_i} - \frac{\alpha}{S} \partial_t \mathbf{S}_i + \frac{\alpha_{\text{sp}}}{S} \mathbf{S}_i \times \boldsymbol{\mu}_i \right), \quad (1)$$

where $\alpha \equiv \alpha_0 + \alpha_{\text{sp}}$ is the sum of the Gilbert damping α_0 and the interfacial Gilbert damping enhancement α_{sp} [20]. Throughout we set $\hbar = 1$. The Hamiltonian is given by

$$\mathcal{H} = -\frac{1}{2} \sum_{ij} [J_{ij} \mathbf{S}_i \cdot \mathbf{S}_j - D_{ij} \hat{\mathbf{z}} \cdot (\mathbf{S}_i \times \mathbf{S}_j)] - H_0 \sum_i S_i^z, \quad (2)$$

where nearest neighbors experience an exchange coupling, $J_{ij} = J$, and next-nearest neighbors are coupled through the Dzyaloshinskii-Moriya interaction (DMI), $D_{ij} = -D_{ji} = D$. The spins are aligned to an external magnetic field applied in the z direction, contributing a Zeeman energy H_0 . Furthermore, $\boldsymbol{\mu}_i = \mu_i \hat{\mathbf{z}}$ is the spin accumulation in the normal metal attached to site i , taken such that

$$\mu_i = \begin{cases} +\mu & i \in \mathcal{A} \\ -\mu & i \in \mathcal{B} \end{cases} \quad (3)$$

changes sign between sublattices \mathcal{A} and \mathcal{B} . We refer to μ as the spin bias throughout this work. The envisioned physical setup for realizing a spin bias as in Eq. (3) depends on the details of the model. For the magnon Haldane model in Eq. (2) with its ground state spin texture oriented out of the plane, the anomalous spin Hall effect [45, 46] can be used to create a spin accumulation at the normal metal to ferromagnet interface. Other realizations of a magnon Chern insulator, such as in-plane field-polarized Kitaev-Heisenberg magnets [47], may require the spin Hall effect to create the spin bias. We note here that one could also choose a spin-orbit torque that only affects one of the sublattice sites, i.e., only $\mu_{i \in \mathcal{A}} \neq 0$. This sublattice-asymmetric setup results in the same topological features that we will discuss below for the sublattice-antisymmetric setup in Eq. (3). For completeness, we discuss the asymmetric setup in the Supplemental Material (SM) [48].

We linearize the LLG equation (1) in deviations $m_i = (S_i^x + iS_i^y)/\sqrt{2S}$ from the uniform state $\mathbf{S}_i = S\hat{\mathbf{z}}$, apply the Fourier transform of the spin-wave operators, $m_{\mathcal{A}/\mathcal{B},i} = \sqrt{2/N} \sum_{\mathbf{k}} e^{i\mathbf{k} \cdot \mathbf{R}_i} m_{\mathcal{A}/\mathcal{B},\mathbf{k}}$ and obtain the equation of motion,

$$i(1 + i\alpha)\partial_t \boldsymbol{\Psi}_{\mathbf{k}} = \mathcal{H}_{\mathbf{k}} \boldsymbol{\Psi}_{\mathbf{k}}, \quad (4)$$

where we have introduced the effective non-Hermitian Hamiltonian matrix

$$\mathcal{H}_{\mathbf{k}} = (H + 3JS)\sigma_0 + \mathbf{h}_{\mathbf{k}} \cdot \boldsymbol{\sigma} + i\gamma\sigma_z. \quad (5)$$

Here $\boldsymbol{\Psi}_{\mathbf{k}} = (m_{\mathcal{A},\mathbf{k}}, m_{\mathcal{B},\mathbf{k}})^T$ is the magnon state vector, $\boldsymbol{\sigma}$ is a pseudovector of Pauli matrices and $\mathbf{h}_{\mathbf{k}}$ comprise the details of the magnon Haldane model, which are detailed in the SM [48]. Furthermore, we have incorporated the spin-orbit torque in the Hamiltonian, resulting in an effective imaginary mass

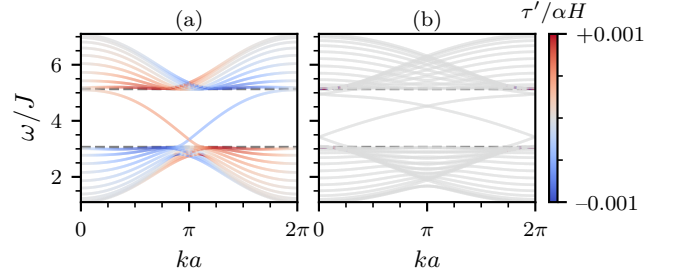


FIG. 2. The bandstructure for a zigzag (a) and armchair nanoribbon (b). The colorscale indicates the lifetime correction τ' induced by the spin bias $\mu/J = 1$. There are bulk lifetime corrections for both the zigzag and armchair edges, but the latter are too small to be visible on the colorscale. The lifetimes of the left- and right-moving edge mode in the zigzag nanoribbon are enhanced and reduced respectively.

$i\gamma\sigma_z$, with $\gamma \equiv \alpha_{\text{sp}}\mu$, which renders the Hamiltonian non-Hermitian.

The stability of this system can be determined by solving Eq. (4) for $\mathbf{k} = 0$ and up to first order in the dissipative terms, α and γ . We then find that $\hbar\omega_{\mathbf{k}=0} = H + 3JS - i\alpha H - \sqrt{9J^2S^2 - \gamma^2}$, and thus the system is stable if $\gamma^2 < 9J^2S^2$. At $\gamma^2 = 9J^2S^2$ there is an exceptional point, signaling an instability [38]. We focus in this work on the stable regime, and choose $|\gamma| < 3JS$.

The Chern number C_n of the n -th band is still well-defined in the presence of the imaginary mass γ , and we find $C_1 = -1$ and $C_2 = 1$, if $D \neq 0$ and $|\gamma|/JS < 1$ [49]. From the bulk-boundary correspondence it thus follows that in the topologically non-trivial phase there exist chiral edge modes for open boundary conditions. However, the finite imaginary mass $i\gamma$ leads to crucial modifications of the chiral edge modes' lifetime and localization, resulting in an enhanced lifetime and localization of the modes on one side of the sample [50].

In what follows, we choose $S = 1$, $D/J = 0.2$, $H = 1.1$, $\alpha_0 = 5 \times 10^{-3}$ and $\alpha_{\text{sp}} = 5 \times 10^{-3}$. We show in Fig. 2 the dispersion of a nanoribbon, chosen with either zigzag or armchair edges along the periodic boundary conditions. The colorscale indicates the lifetime correction, $\tau' \equiv -\text{Im}[\epsilon]$, where ϵ is the complex energy obtained from diagonalizing the effective non-Hermitian Hamiltonian. We emphasize that our calculation include the fact that boundary spins have a lower coordination number than the bulk spins, effectively reducing the on-site potential on the edge [51, 52].

For the zigzag edges, Fig. 2(a), the left-moving modes have an increased lifetime, because they have support on the \mathcal{A} -sites, which have a positive spin bias applied. In contrast, the right-moving modes have a reduced lifetime, because of their support on the \mathcal{B} -sites, where a negative spin bias applied. Left-moving edge modes are therefore amplified relative to right-moving edge modes. The bulk modes also have lifetime corrections, but since the edge states are topologically protected and thus robust to disorder, we expect that a realistic level of disorder will reduce the bulk mode lifetime, while the edge modes remain protected. We will return to the effect

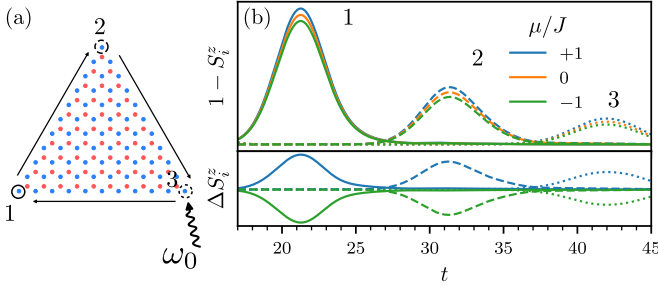


FIG. 3. The same as Fig. 1, but for a triangle configuration chosen such that all edges are of the zigzag type *and* amplifying for $\mu > 0$. Note that the excitation happens at a site also used for detection (site 3).

of disorder in the context of spin transport below.

In contrast, the left- and right-moving modes of the armchair nanoribbon, Fig. 2(b), are not amplified. There are small lifetime corrections to the bulk modes—too small to be visible on this color scale—but again, we do not expect these corrections to be robust against disorder. Instead, for the armchair edges, the effect of the spin-orbit torque manifests itself as a hybrid skin-effect, which localizes the edge modes on one side of the sample [49, 50, 53, 54]. We focus on the amplification in the main text, and discuss the hybrid skin-effect in more detail in the SM [48].

Numerical LLG simulations. Having established the amplification under periodic boundary conditions within linear spin-wave theory, we now turn our attention to a finite-size system and demonstrate these effects by numerical LLG simulations. In these simulations, we initialize the system in the uniform state $\mathbf{S}_i = S \hat{z}$ and excite an edge mode at time $t = 0$ at a site on the edge, with a frequency $\omega_0/J = 3.8$ in the gap. We then track the spin-wave amplitude, defined as $1 - S_i^z$, at selected sites at the edge at a distance from the excitation point. Below, we refer to these measuring points as “detectors.” We discuss further details of the simulations in the SM [48].

We first consider a rectangle, with approximately similar lengths of armchair and zigzag edges, and we show the detected signal in Fig. 1(b). Upon excitation, the edge mode travels around the system, arriving at the first detector after a characteristic time determined by the group velocity of the excited mode. The edge mode has now traveled through a zigzag edge, so the signal is either amplified or suppressed, depending on the sign of the spin bias μ . Next, the mode passes through an armchair edge, which does not amplify the mode—as indicated by the fact that the splitting remains constant between the first and second detector. Finally, the mode travels through a zigzag edge with an opposite orientation to the first zigzag edge. Therefore, the modes that were previously amplified are now suppressed, and vice versa. This can be observed by the lack of splitting when the mode arrives at the third detector—effectively cancelling out the amplification of the first zigzag edge.

In addition, it is possible to design a triangle oriented such that all of its edges are of the zigzag type and terminated pre-

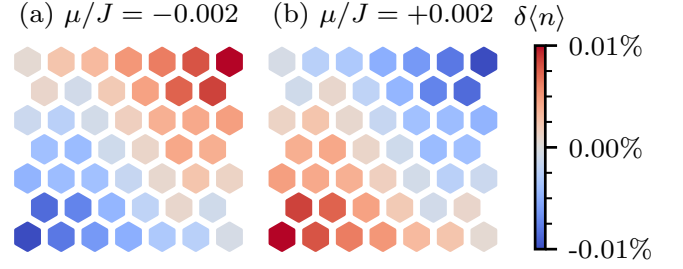


FIG. 4. The relative change in magnon occupation, for opposite values of the spin bias μ/J : (a) -0.002 and (b) $+0.002$, summed over a hexagon containing three \mathcal{A} and three \mathcal{B} sites. The sign of spin bias determines the localization of the edge modes on the top or bottom zigzag edge.

dominantly by \mathcal{A} -sites. Therefore, each edge amplifies the mode, resulting in a recurrent amplification as the mode travels around the system. This setup is shown in Fig. 3, where the splitting is present at all detectors. Note however that due to the finite Gilbert damping in the system, the growth is bounded.

Magnon density. We propose that the amplification can also be measured directly by probing the average magnon density $\langle n_i \rangle$, for example by nitrogen-vacancy magnetometry [55]. To model this, we add a stochastic magnetic field \mathbf{h}_i to the LLG equation (1), representing thermal fluctuations that are fixed by the quantum-mechanical fluctuation-dissipation theorem (FDT) [56–58]. These fields allow us to accurately describe the thermal population of magnons, including the fluctuations due to the interface of the ferromagnet with the normal metal, which induces the spin-orbit torque. It is important to note that for the system to be stable in the presence of fluctuations, we require that $\mu_i < H$, i.e., the spin accumulation in the attached normal metal cannot be larger than the lowest magnon band. We choose $\mu/J = \pm 0.002$, which satisfies the stability requirement since $H/J = 1.1$, and $J/T = 1$. Here the spin accumulation is small compared to the temperature, i.e., $|\mu|/T \ll 1$, which we expect to apply to any real system at room temperature. We discuss in the SM [48] the case the spin accumulation is comparable to the temperature.

In Fig. 4 we show the relative change, $\delta\langle n \rangle$, between the cases with and without spin bias. We observe that depending on the sign of the spin bias μ , the magnon density increases or decreases on opposite corners of the lattice. This we attribute to the amplification of the zigzag edges, which transport spin towards these corners. We therefore conclude that the magnon density is a good measure of the amplification, especially since the spin accumulation can be electrically controlled—allowing a single experimental setup to switch between the cases presented in Fig. 4.

Transport. The chiral edge states in the magnon Chern insulator are particularly interesting for highly efficient spin transport [17]. Therefore, we consider spin transport through the zigzag edges to study if it can be electrically controlled. We consider a propagating spin wave experiment as shown in

Fig. 5(a), where magnons are excited with a microwave antenna, and detected with a normal metal strip. We thus add an excitation field, $\mathbf{h}_i^{\text{exc}} = h(\cos(\omega_0 t), \sin(\omega_0 t), 0)$ to the sites in contact with the microwave antenna, with strength h and frequency ω_0 . The excited spin waves travel through the system, and are picked up by a normal metal lead. The spin bias is non-zero only between the injector and the detector [see green region in Fig. 5(a)], such that detection and excitation are performed in the Hermitian phase of the magnon Chern insulator.

The observable in this system is the total spin injected in the right lead. Note that at finite temperatures there will also be spin injected in the lead because of the thermal population of the magnons, but this effect can easily be subtracted experimentally. We thus focus on the zero temperature limit, $T = 0$. We show the technical details of the transport calculation in the SM [48].

One key feature of topological edge modes is their robustness against disorder. We therefore implement disorder in our discrete lattice model by adding a random on-site magnetic field drawn from a uniform distribution in the interval $[-\delta/2, \delta/2]$. We calculate transport through a zigzag-terminated nanoribbon of length $d/a = 200$, because the zigzag edges are capable of amplification of the edge modes. In the calculations that follow, we always consider a finite disorder level of $\delta/J = 1$ (which is chosen such that, since $H = 1.1$, all magnon energies remain positive) and we show results for varying levels of disorder in the SM [48].

The resulting spin current injected in the right lead is depicted in Fig. 5(b) for $\mu/J = \pm 1$ and $\mu = 0$, for the topological trivial ($D = 0$) and non-trivial ($D/J = 0.2$) system. Firstly, we observe that in the topologically trivial case, $D = 0$, there is no notable amplification of the signal for $\mu/J = \pm 1$ compared to $\mu = 0$. However, for the non-trivial case, $D \neq 0$, we observe an amplification or damping, depending on the sign of the spin bias μ . This result is in direct agreement with the amplification found in the numerical Landau-Lifshitz-Gilbert simulations (recall Fig. 1). The amplification or damping is strongest for excitation frequencies in the gap and we thus attribute it to the amplification or damping of the topologically protected edge modes. Since we have included a finite disorder level, we can draw the conclusion that the amplification of the edge modes is robust against disorder. On the contrary, the amplification or damping of the bulk modes is strongly suppressed, and can be effectively ignored.

Finally, we investigate the distance dependence of the amplified signal in Fig. 5(c), where we define the amplification factor $\Delta I \equiv I^{+\mu} - I^{-\mu}$ as the difference in signal between opposite signs of spin biases. We first observe that only the edge modes show notable amplification. Secondly, the signal carries much farther for excitation frequencies in the gap, as is to be expected from the topological protection of these modes, since the finite disorder suppresses the transport of the bulk modes. The effects of disorder are further studied in the SM, where we consider varying levels of disorder [48]. Furthermore, the amplification of the edge modes is strongest for ex-

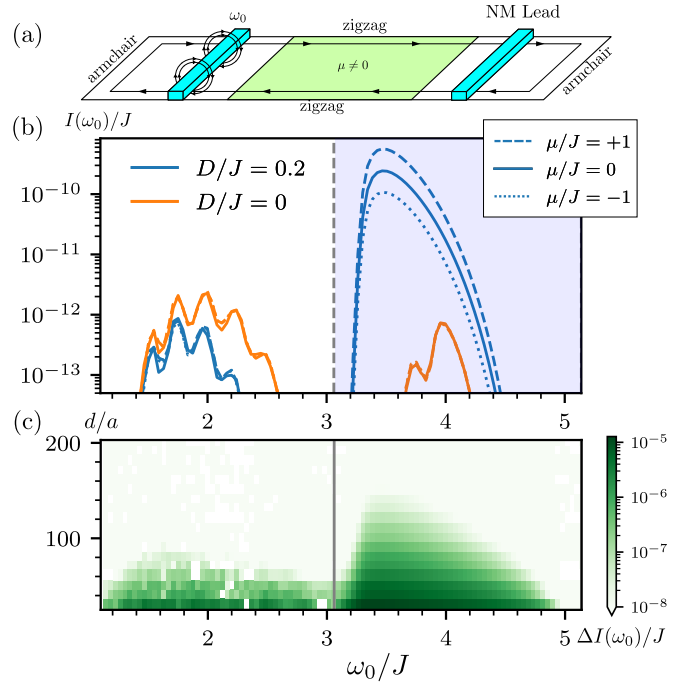


FIG. 5. (a) The transport setup considered. Magnons are excited with a transversely oscillating magnetic field in the left antenna and are detected through spin pumping into a normal metal lead on the right. We consider the transport through zigzag edges, which show amplification. (b) The injected spin current in the right lead, $I(\omega_0)$, as a function of excitation frequency ω_0 , at a fixed distance $d/a = 200$ comparing the topologically trivial ($D = 0$) and topologically non-trivial ($D/J = -0.2$) case and the effects of μ . The shaded area indicates the magnon gap, i.e., where the edge modes reside. (c) For $D/J = 0.2$ and $|\mu|/J = 1$, the spin current difference $\Delta I \equiv I^{+\mu} - I^{-\mu}$ between opposite signs of μ , as a function of distance, d , and excitation frequency, ω_0 .

citation frequencies in the lower part of the topological band gap (around $\omega_0/J \approx 3.5$), which can be explained by the fact that the damping rate in the Gilbert damping description is proportional to frequency, thus suppressing the transport at higher frequencies.

Conclusion and experimental realization. We have shown in this work that the chiral edge states in the magnon Haldane model can be electrically controlled through applying a spin-orbit torque. For the zigzag edge geometry this results in an amplification of the edge modes, which we have confirmed using numerical Landau-Lifshitz-Gilbert simulations. In addition, this amplification is reflected in the magnon density, increasing the magnon density on one side of the sample. Finally, we have shown this enhanced transport to be robust against disorder within the linear spin-wave theory formalism, indicating that amplification over large distances is a possibility.

To realize the non-Hermitian topological magnon phase considered in this work, we foresee two possibilities: (i) certain magnetic compounds and (ii) artificial magnetic materials. For the first, the sublattice-dependent SOT as considered

in this work can be realized in specific ferromagnetic van der Waals materials with a buckled honeycomb structure, such that the \mathcal{A} - and \mathcal{B} -sites couple asymmetrically to normal metal layers above and below. Secondly, the site-dependent SOT could also be realized in artificial magnetic materials, such as topological magnonic crystals [4, 59] and magnetic solitons in a honeycomb lattice [60]. Importantly, these artificial materials would offer remarkable control over both the driving and the edge geometry.

Finally, we reiterate that the topological features discussed in this work are unchanged for a sublattice-asymmetric setup instead of the antisymmetric setup proposed in Eq. (3), such that only the \mathcal{A} -sites are driven by a spin-orbit torque. In particular, we believe that this would be experimentally easier to realize. In the SM [48] we have explored this in more detail, reproducing the calculations shown in this work for the asymmetric spin-orbit torque.

Acknowledgments. This work is in part funded by the Fluid Spintronics research program with Project No. 182.069, financed by the Dutch Research Council (NWO), and by the Deutsche Forschungsgemeinschaft (DFG, German Research Foundation) – Project No. 504261060 (Emmy Noether Programme).

* pgunnink@uni-mainz.de

- [1] A. V. Chumak, V. I. Vasyuchka, A. A. Serga, and B. Hillebrands, Magnon spintronics, *Nature Physics* **11**, 453 (2015).
- [2] H. Katsura, N. Nagaosa, and P. A. Lee, Theory of the Thermal Hall Effect in Quantum Magnets, *Physical Review Letters* **104**, 066403 (2010).
- [3] K. A. van Hoogdalem, Y. Tserkovnyak, and D. Loss, Magnetic texture-induced thermal Hall effects, *Physical Review B* **87**, 024402 (2013).
- [4] R. Shindou, R. Matsumoto, S. Murakami, and J.-i. Ohe, Topological chiral magnonic edge mode in a magnonic crystal, *Physical Review B* **87**, 174427 (2013).
- [5] L. Zhang, J. Ren, J.-S. Wang, and B. Li, Topological magnon insulator in insulating ferromagnet, *Physical Review B* **87**, 144101 (2013).
- [6] A. Mook, J. Henk, and I. Mertig, Edge states in topological magnon insulators, *Physical Review B* **90**, 024412 (2014).
- [7] S. A. Owerre, A first theoretical realization of honeycomb topological magnon insulator, *Journal of Physics: Condensed Matter* **28**, 386001 (2016).
- [8] S. K. Kim, H. Ochoa, R. Zarzuela, and Y. Tserkovnyak, Realization of the Haldane-Kane-Mele Model in a System of Localized Spins, *Physical Review Letters* **117**, 227201 (2016).
- [9] A. Mook, K. Plekhanov, J. Klinovaja, and D. Loss, Interaction-Stabilized Topological Magnon Insulator in Ferromagnets, *Physical Review X* **11**, 021061 (2021).
- [10] K. Nakata, S. K. Kim, J. Klinovaja, and D. Loss, Magnonic topological insulators in antiferromagnets, *Physical Review B* **96**, 224414 (2017).
- [11] A. Mook, B. Göbel, J. Henk, and I. Mertig, Taking an electron-magnon duality shortcut from electron to magnon transport, *Physical Review B* **97**, 140401(R) (2018).
- [12] H. Kondo, Y. Akagi, and H. Katsura, F_2 topological Invariant for Magnon Spin Hall Systems, *Physical Review B* **99**, 041110(R) (2019).
- [13] J. Fransson, A. M. Black-Schaffer, and A. V. Balatsky, Magnon Dirac materials, *Physical Review B* **94**, 075401 (2016).
- [14] S. S. Pershoguba, S. Banerjee, J. C. Lashley, J. Park, H. Ågren, G. Aepli, and A. V. Balatsky, Dirac Magnons in Honeycomb Ferromagnets, *Physical Review X* **8**, 011010 (2018).
- [15] F.-Y. Li, Y.-D. Li, Y. B. Kim, L. Balents, Y. Yu, and G. Chen, Weyl magnons in breathing pyrochlore antiferromagnets, *Nature Communications* **7**, 12691 (2016).
- [16] A. Mook, J. Henk, and I. Mertig, Tunable Magnon Weyl Points in Ferromagnetic Pyrochlores, *Physical Review Letters* **117**, 157204 (2016).
- [17] A. Rückriegel, A. Brataas, and R. A. Duine, Bulk and edge spin transport in topological magnon insulators, *Physical Review B* **97**, 081106(R) (2018).
- [18] X. S. Wang, A. Brataas, and R. E. Troncoso, Bosonic Bott Index and Disorder-Induced Topological Transitions of Magnons, *Physical Review Letters* **125**, 217202 (2020).
- [19] Y. Tserkovnyak, A. Brataas, and G. E. W. Bauer, Spin pumping and magnetization dynamics in metallic multilayers, *Physical Review B* **66**, 224403 (2002).
- [20] Y. Tserkovnyak, A. Brataas, and G. E. W. Bauer, Enhanced Gilbert Damping in Thin Ferromagnetic Films, *Physical Review Letters* **88**, 117601 (2002).
- [21] Y. Tserkovnyak, A. Brataas, G. E. W. Bauer, and B. I. Halperin, Nonlocal magnetization dynamics in ferromagnetic heterostructures, *Reviews of Modern Physics* **77**, 1375 (2005).
- [22] A. Houshang, E. Iacocca, P. Dürrenfeld, S. R. Sani, J. Åkerman, and R. K. Dumas, Spin-wave-beam driven synchronization of nanocontact spin-torque oscillators, *Nature Nanotechnology* **11**, 280 (2016).
- [23] Y. Tserkovnyak, Exceptional points in dissipatively coupled spin dynamics, *Physical Review Research* **2**, 013031 (2020).
- [24] H. Y. Yuan, R. Lavrijsen, and R. A. Duine, Unidirectional magnetic coupling induced by chiral interaction and nonlocal damping, *Physical Review B* **107**, 024418 (2023).
- [25] X. Li, M. A. Begaowe, S. Zhang, and B. Flebus, *Reciprocal Reservoir Induced Non-Hermitian Skin Effect* (2023), [arxiv:2307.15792](https://arxiv.org/abs/2307.15792) [cond-mat, physics:quant-ph].
- [26] J. C. Slonczewski, Current-driven excitation of magnetic multilayers, *Journal of Magnetism and Magnetic Materials* **159**, L1 (1996).
- [27] L. Berger, Emission of spin waves by a magnetic multilayer traversed by a current, *Physical Review B* **54**, 9353 (1996).
- [28] P. M. Gunnink, J. S. Harms, R. A. Duine, and A. Mook, Zero-Frequency Chiral Magnonic Edge States Protected by Nonequilibrium Topology, *Physical Review Letters* **131**, 126601 (2023).
- [29] K. An, D. R. Birt, C.-F. Pai, K. Olsson, D. C. Ralph, R. A. Buhrman, and X. Li, Control of propagating spin waves via spin transfer torque in a metallic bilayer waveguide, *Physical Review B* **89**, 140405 (2014).
- [30] L. J. Cornelissen, J. Liu, B. J. van Wees, and R. A. Duine, Spin-Current-Controlled Modulation of the Magnon Spin Conductance in a Three-Terminal Magnon Transistor, *Physical Review Letters* **120**, 097702 (2018).
- [31] J. Liu, X.-Y. Wei, G. E. W. Bauer, J. B. Youssef, and B. J. van Wees, Electrically induced strong modulation of magnon transport in ultrathin magnetic insulator films, *Physical Review B* **103**, 214425 (2021).
- [32] Z. Gong, Y. Ashida, K. Kawabata, K. Takasan, S. Higashikawa, and M. Ueda, Topological Phases of Non-Hermitian Systems, *Physical Review X* **8**, 031079 (2018).
- [33] K. Kawabata, K. Shiozaki, M. Ueda, and M. Sato, Symmetry

- and Topology in Non-Hermitian Physics, *Physical Review X* **9**, 041015 (2019).
- [34] E. J. Bergholtz, J. C. Budich, and F. K. Kunst, Exceptional topology of non-Hermitian systems, *Reviews of Modern Physics* **93**, 015005 (2021).
 - [35] M. A. Bandres, S. Wittek, G. Harari, M. Parto, J. Ren, M. Segev, D. N. Christodoulides, and M. Khajavikhan, Topological insulator laser: Experiments, *Science* **359**, eaar4005 (2018).
 - [36] G. Harari, M. A. Bandres, Y. Lumer, M. C. Rechtsman, Y. D. Chong, M. Khajavikhan, D. N. Christodoulides, and M. Segev, Topological insulator laser: Theory, *Science* **359**, eaar4003 (2018).
 - [37] P. A. McClarty and J. G. Rau, Non-Hermitian topology of spontaneous magnon decay, *Physical Review B* **100**, 100405 (2019).
 - [38] K. Deng, X. Li, and B. Flebus, Exceptional points as signatures of dynamical magnetic phase transitions, *Physical Review B* **107**, L100402 (2023).
 - [39] K. Deng and B. Flebus, Non-Hermitian skin effect in magnetic systems, *Physical Review B* **105**, L180406 (2022).
 - [40] B. Flebus, R. A. Duine, and H. M. Hurst, Non-Hermitian topology of one-dimensional spin-torque oscillator arrays, *Physical Review B* **102**, 180408 (2020).
 - [41] P. M. Gunnink, B. Flebus, H. M. Hurst, and R. A. Duine, Non-linear dynamics of the non-Hermitian Su-Schrieffer-Heeger model, *Physical Review B* **105**, 104433 (2022).
 - [42] H. M. Hurst and B. Flebus, Non-Hermitian physics in magnetic systems, *Journal of Applied Physics* **132**, 220902 (2022).
 - [43] X. Li, K. Deng, and B. Flebus, Multitude of exceptional points in van der Waals magnets, *Physical Review B* **106**, 214432 (2022).
 - [44] T. Yu, J. Zou, B. Zeng, J. W. Rao, and K. Xia, *Non-Hermitian Topological Magnonics* (2023), [arxiv:2306.04348 \[cond-mat\]](https://arxiv.org/abs/2306.04348).
 - [45] K. S. Das, W. Y. Schoemaker, B. J. van Wees, and I. J. Vera-Marun, Spin injection and detection via the anomalous spin Hall effect of a ferromagnetic metal, *Physical Review B* **96**, 220408(R) (2017).
 - [46] K. S. Das, J. Liu, B. J. van Wees, and I. J. Vera-Marun, Efficient Injection and Detection of Out-of-Plane Spins via the Anomalous Spin Hall Effect in Permalloy Nanowires, *Nano Letters* **18**, 5633 (2018).
 - [47] E. Z. Zhang, L. E. Chern, and Y. B. Kim, Topological magnons for thermal Hall transport in frustrated magnets with bond-dependent interactions, *Physical Review B* **103**, 174402 (2021).
 - [48] See Supplemental Material for the details of the spin-wave Hamiltonian, the details of the magnon density calculations, a discussion on the hybrid skin-effect, details of the numerical LLG simulations, details of the transport calculations, including the effects of disorder, and further results showing the effect of an asymmetric spin-orbit torque.
 - [49] Y. Li, C. Liang, C. Wang, C. Lu, and Y.-C. Liu, Gain-Loss-Induced Hybrid Skin-Topological Effect, *Physical Review Letters* **128**, 223903 (2022).
 - [50] W. Zhu and J. Gong, Hybrid skin-topological modes without asymmetric couplings, *Physical Review B* **106**, 035425 (2022).
 - [51] P. A. Pantaleón and Y. Xian, Effects of Edge on-Site Potential in a Honeycomb Topological Magnon Insulator, *Journal of the Physical Society of Japan* **87**, 064005 (2018).
 - [52] S. S. Pershoguba, S. Banerjee, J. C. Lashley, J. Park, H. Ågren, G. Aepli, and A. V. Balatsky, Dirac Magnons in Honeycomb Ferromagnets, *Physical Review X* **8**, 011010 (2018).
 - [53] F. K. Kunst, E. Edvardsson, J. C. Budich, and E. J. Bergholtz, Biorthogonal Bulk-Boundary Correspondence in Non-Hermitian Systems, *Physical Review Letters* **121**, 026808 (2018).
 - [54] N. Okuma, K. Kawabata, K. Shiozaki, and M. Sato, Topological Origin of Non-Hermitian Skin Effects, *Physical Review Letters* **124**, 086801 (2020).
 - [55] L. Rondin, J.-P. Tetienne, T. Hingant, J.-F. Roch, P. Maletinsky, and V. Jacques, Magnetometry with nitrogen-vacancy defects in diamond, *Reports on Progress in Physics* **77**, 056503 (2014).
 - [56] A. Brataas, H. Skarsvåg, E. G. Tveten, and E. Løhaugen Fjærbu, Heat transport between antiferromagnetic insulators and normal metals, *Physical Review B* **92**, 180414 (2015).
 - [57] S. A. Bender, H. Skarsvåg, A. Brataas, and R. A. Duine, Enhanced Spin Conductance of a Thin-Film Insulating Antiferromagnet, *Physical Review Letters* **119**, 056804 (2017).
 - [58] J. Zheng, S. Bender, J. Armitis, R. E. Troncoso, and R. A. Duine, Green's function formalism for spin transport in metal-insulator-metal heterostructures, *Physical Review B* **96**, 174422 (2017).
 - [59] R. Shindou, J.-i. Ohe, R. Matsumoto, S. Murakami, and E. Saitoh, Chiral spin-wave edge modes in dipolar magnetic thin films, *Physical Review B* **87**, 174402 (2013).
 - [60] S. K. Kim and Y. Tserkovnyak, Chiral Edge Mode in the Coupled Dynamics of Magnetic Solitons in a Honeycomb Lattice, *Physical Review Letters* **119**, 077204 (2017).

Supplemental Material: Electrical Non-Hermitian Control of Topological Magnon Spin Transport

DETAILS OF THE HALDANE MODEL

Upon linearization, $m_i = (S_i^x + iS_i^y)/\sqrt{2S}$, of the Landau-Lifshitz-Gilbert equation [Eq. (1) in the main text], in combination with the Hamiltonian [Eq. (2) in the main text], we obtain the equation of motion

$$i(1 + i\alpha)\partial_t m_i = \sum_j H_{ij} m_j \quad (\text{S1})$$

where

$$H_{ij} = \delta_{ij} \left(H + S \sum_n J_{in} + i\gamma_j \right) - S(J_{ij} + iD_{ij}) \quad (\text{S2})$$

is the linear spin-wave Hamiltonian and $\gamma_i \equiv \alpha\mu_i$.

We introduce the Fourier transform of the spin-wave operators, $m_{\mathcal{A}/\mathcal{B},i} = \sqrt{2/N} \sum_{\mathbf{k}} e^{i\mathbf{k} \cdot \mathbf{R}_i} m_{\mathcal{A}/\mathcal{B},\mathbf{k}}$ for the sublattices \mathcal{A}/\mathcal{B} respectively, and obtain the equation of motion [Eq. (4) in the main text], with the Hamiltonian given by Eq. (5) in the main text. Additionally, we have defined

$$\mathbf{h}_{\mathbf{k}} = S \sum_i \begin{pmatrix} -J \cos(\mathbf{k} \cdot \boldsymbol{\delta}_i) \\ J \sin(\mathbf{k} \cdot \boldsymbol{\delta}_i) \\ 2D \sin(\mathbf{k} \cdot \boldsymbol{\rho}_i) \end{pmatrix}, \quad (\text{S3})$$

where $\boldsymbol{\delta}_i$ and $\boldsymbol{\rho}_i$ are the vectors connecting nearest and next-nearest neighbors respectively.

DETAILS OF CALCULATIONS FOR THE MAGNON DENSITY

To calculate the magnon density, we add to the LLG equation a magnetic field \mathbf{h}_i , modelling stochastic fluctuations, such that $\partial_t \mathbf{S}_i|_{\text{stoch}} = -\mathbf{S}_i \times \mathbf{h}_i$. After linearization, we Fourier transform the equation of motion [Eq. S1] to frequency space, to obtain

$$\sum_j \mathbb{G}_{ij}^{-1}(\omega) m_j(\omega) = h_i^0(\omega) + h_i^{\text{sp}}(\omega). \quad (\text{S4})$$

Here, $h_i^{0/\text{sp}}(\omega)$ is the Fourier transform of the circular components $h_i^{0/\text{sp}} = h_i^x + ih_i^y$ of the stochastic magnetic field, taking into account the fluctuations related to the bulk Gilbert damping (h_i^0) and the interfacial spin-pumping (h_i^{sp}). The inverse magnon propagator is given by $\mathbb{G}_{ij}^{-1}(\omega) = -\delta_{ij}(1 + i\alpha)\omega + H_{ij}$, where H_{ij} is the effective non-Hermitian Hamiltonian in real space,

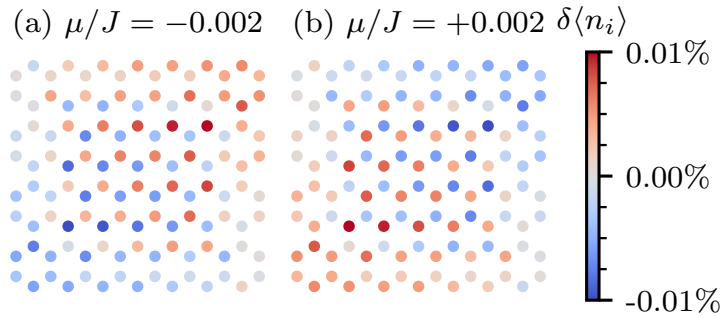


FIG. S1. The relative site-resolved change of magnon density, before spatial averaging. Parameters are identical to Fig. 4 in the main text. The magnon density changes between the \mathcal{A} and \mathcal{B} sites, and thus the build up of spin is hard to observe. After averaging one sees the build up of spin more clearly, cf. Fig. 4 in the main text.

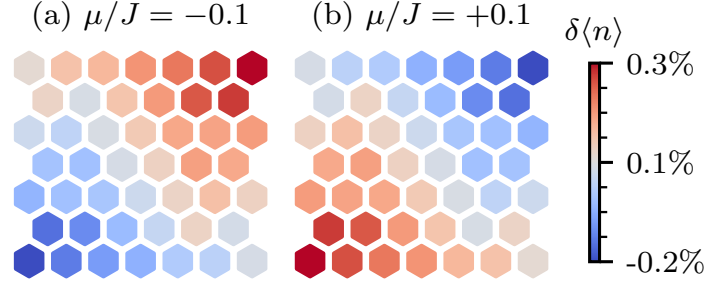


FIG. S2. The relative magnon density with $\mu/J = 0.1$ and $T/J = 1$, for opposite values of the spin bias μ/J . Other parameters are identical to Fig. 4 in the main text. Importantly, the overall average magnon density increases and is no longer symmetric around $\delta\langle n \rangle = 0$, which we attribute to quantum-mechanical corrections to the FDT, since here μ is comparable to the temperature T .

given by Eq. (S2). At finite temperatures, the stochastic magnetic field $h_i(\omega)$ has to be chosen such that $\langle h_i(\omega) \rangle = 0$ and $\langle h_i^{0/sp}(\omega) h_j^{0/sp}(\omega')^* \rangle = 2\pi\delta(\omega - \omega') \mathbb{R}_{ij}^{0/sp}(\omega)$, where

$$\mathbb{R}_{ij}^0(\omega) = \delta_{ij} \frac{4\alpha_0\omega/S}{e^{\omega/k_B T} - 1} \quad \text{and} \quad \mathbb{R}_{ij}^{sp}(\omega) = \delta_{ij} \frac{4\alpha_{sp}(\omega - \mu_i)/S}{e^{(\omega - \mu_i)/k_B T} - 1} \quad (\text{S5})$$

are covariance matrices determined by the quantum-mechanical fluctuation-dissipation theorem to ensure agreement with the quantum-mechanical linear spin-wave theory for magnons [56–58].

The average magnon number, $\langle n_i \rangle$, of the local spin i , can then be found as

$$\langle n_i \rangle = \int \frac{d\omega}{2\pi} \left\{ \mathbb{G}(\omega) \left[\mathbb{R}^0(\omega) + \mathbb{R}^{sp}(\omega) \right] \mathbb{G}^\dagger(\omega) \right\}_{ii}. \quad (\text{S6})$$

To highlight the relative change of $\langle n_i \rangle$ under the spin bias μ , we show in the main text

$$\delta\langle n_i \rangle \equiv \frac{\langle n_i \rangle_{\mu=0} - \langle n_i \rangle}{\langle n_i \rangle_{\mu=0}} \times 100\%, \quad (\text{S7})$$

i.e., the relative change of magnon density as the spin bias is turned on. Because the site-resolved occupation is strongly dependent on the on-site spin bias, we average over a hexagon containing three \mathcal{A} and three \mathcal{B} sites. We note that one single site can be part of up to three hexagons. For completeness, we shown in Fig. S1 the change in magnon density without this averaging procedure.

The stochastic magnetic fields in Eq. (S5) follow from with the quantum-mechanical FDT. We expect the quantum-mechanical nature of the FDT to become relevant if the spin accumulation is comparable to the temperature energy scale. In the main text, we have chosen $|\mu|/J = 0.002$, and we therefore do not expect such corrections there. To demonstrate that the quantum-mechanical nature of the FDT becomes relevant for large μ , we choose $\mu/J = 0.1$ (as a reminder, $T/J = 1$), and show the resulting magnon density in Fig. S2. We observe that the magnon density on average increases for both positive and negative spin bias μ , which we therefore attribute to the quantum-mechanical FDT. In realistic system at room temperature however, we do not expect the spin accumulation to be comparable to the temperature energy scale, and we thus concentrate on $\mu/T \ll 1$ when discussing the magnon density in the main text.

HYBRID SKIN-EFFECT

Besides lasing, the model as considered here also exhibits the hybrid skin-effect, which we discuss here in more detail. Importantly, this hybrid skin-effect manifests itself only for nanoribbons with an armchair edge. For nanoribbons with a zigzag edge, the edge modes are localized symmetrically on either the top or bottom: the left-moving mode is localized on one side, the right-moving mode on the other side of the ribbon. To demonstrate this, we show in Fig. 2(b-c) the localization of the eigenmodes. Because we sit exactly at the point where the two edge modes cross, we obtain linear combinations of the left-moving mode and right-moving mode, which are localized on opposite sides of the sample. Therefore, the eigenmodes are distributed throughout the nanoribbon. We confirm this by calculating the spatially asymmetric part of the eigenmodes, defined as $\Delta|\psi|^2 \equiv |\psi_t|^2 - |\psi_b|^2$, where $\psi_{t,b}$ are the top and bottom parts of the eigenmodes, corresponding to the energies indicated by the

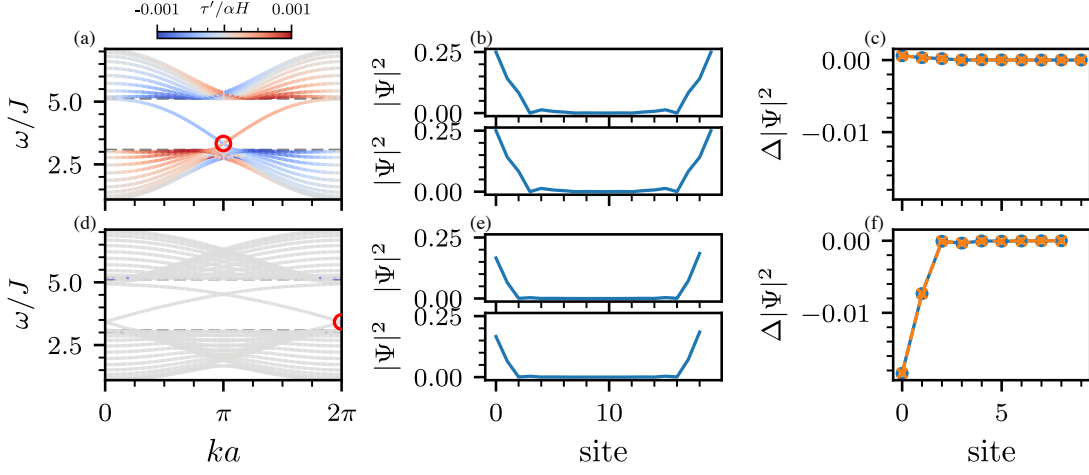


FIG. S3. For a zigzag (top row) and armchair nanoribbon (bottom row) the magnon dispersion (a,d), the localization of the eigenmodes circled in red (b,e) and the corresponding spatially asymmetric part of the eigenmodes $\Delta|\psi|^2$ (c,f)). The colorscale in (a,d) indicates the lifetime correction τ' induced by the spin bias $\mu/J = 1$. The lifetimes of the left- and right-moving edge mode in the zigzag nanoribbon are enhanced and reduced respectively, whereas in the armchair nanoribbon the edge modes exhibit the hybrid skin-effect and are thus localized on one side of the sample.

red circle. We observe here no noticeable localization of the eigenmodes, especially when comparing to the armchair nanoribbon, which we discuss next.

For the armchair ribbon, the eigenmodes, Fig. 2(e-f), $|\psi|^2$ have an asymmetric distribution in space, and are localized on one side of the sample. This change is too small to observe in Fig. 2(e), but is clearly present in the spatially asymmetric part of the eigenmodes shown in Fig. 2(f). Therefore, the eigenmodes are both localized on the top of the sample and the armchair edge modes thus exhibit a *hybrid* skin-effect. The skin effect generally refers to the localization of eigenmodes on one side of the sample [53, 54], but here the localization is only present for edge modes in the armchair geometry. We therefore refer to this as the hybrid skin-effect, as suggested by Refs. [49, 50], who first discovered this effect. Not shown here are the bulk modes, but we have confirmed that these do not exhibit this asymmetric localization. Finally, we note that the asymmetric localization of the magnon density discussed in the main text, is the equivalent of the hybrid skin-effect discussed here, but for open boundary conditions [49].

In the zigzag orientation there is no hybrid skin-effect, there is a lasing of the edge modes—which has the same physical origin, namely the non-Hermitian topology. Both effects are therefore two sides of the same coin, manifested differently under different boundary conditions.

DETAILS OF NUMERICAL LANDAU-LIFSHITZ-GILBERT SIMULATIONS

We describe here the details for numerically solving the Landau-Lifshitz-Gilbert equation [Eq. (1) in the main text]. A spin wave is excited with a pulse of a local transversely oscillating magnetic field $\mathbf{h}_e = b_0 f_e(t)(\cos \omega_0 t \hat{x} + \sin \omega_0 t \hat{y})$ added to the LLG equation, such that $\partial_t \mathbf{S}_{i|e} = -\delta_{in} \mathbf{S}_i \times \mathbf{h}_e$, where n is the excitation site. Here $f_e(t) = \exp[-(t-b)^2/2c^2]$ is an envelope function which slowly turns the pulse on and off, since turning on the excitation pulse instantaneously will excite a range of spurious frequencies. We have chosen $b = 4.5J^{-1}$, $c = 3J^{-1}$ and $b_0/S = 5 \times 10^{-3}$. At $t = 0$ all spins are aligned along the z directions, and the LLG equation is numerically solved with timesteps of $\Delta t = 0.01J^{-1}$.

DETAILS OF TRANSPORT CALCULATIONS

We consider in the main text a transport setup as shown in Fig. 5 in the main text. Magnons are excited by an antenna on the left side, travel through a nanoribbon oriented such that the transport occurs parallel to the zigzag edge, and inject spin into an attached normal metal right side. We model this by taking a nanoribbon of length d , and add a local driving field $h_i^{\text{exc}} = b_0 \cos \omega_0 t \hat{x} \delta_{i \in \text{antenna}}$ to the leftmost sites. To the rightmost sites we add a normal metal lead. In order to minimize reflections, we add an interfacial Gilbert damping enhancement α_{IF} to the left- and rightmost sites. For the sites between the left antenna and right normal metal lead we allow for $\mu \neq 0$, whilst $\mu = 0$ for the sites in contact with the left antenna and right

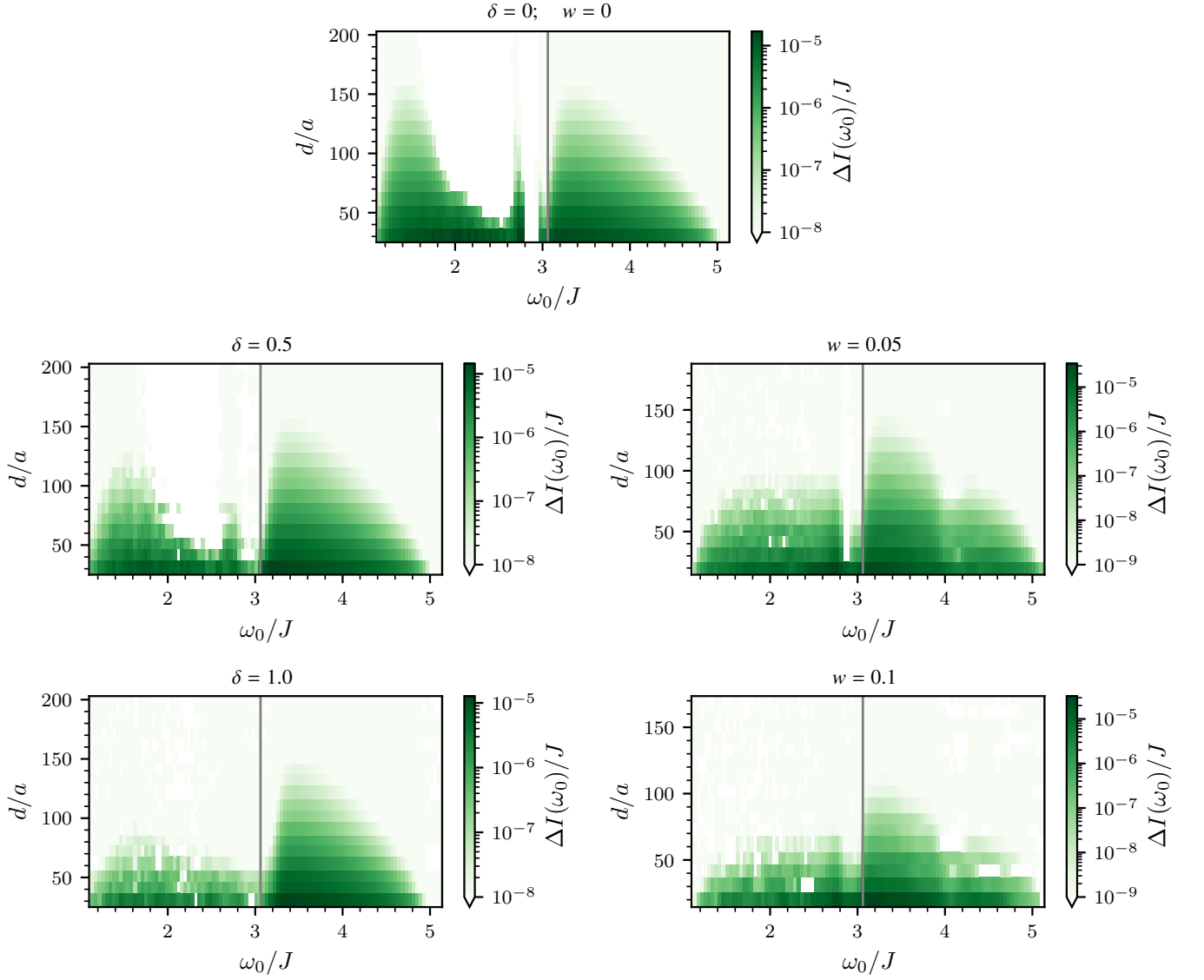


FIG. S4. The spin transport amplification factor ΔI as a function of antenna distance d and excitation frequency ω_0 for selected disorder concentrations. δ denotes the random on-site potential, and w the defect concentration. (Top) No disorder, $\delta = w = 0$. (Left panels) Only random on-site potential disorder. (Right panels) Only defect concentration. In both cases, for increasing disorder, the bulk signal is suppressed, while the signal carried by the edge modes is more robust. Note that the color scales are not equivalent for each figure. Also, this is a logarithmic color scale, and thus negative values of ΔI (which are possible in the presence of disorder) are represented as white.

normal metal. The detection and injection therefore happens in the Hermitian phase, but transport happens in the non-Hermitian phase.

Similar to Eq. (S4), the equation of motion for this system is given by

$$\sum_j \mathbb{G}_{ij}^{-1}(\omega) m_j(\omega) = h_i^{\text{exc}}(\omega), \quad (\text{S8})$$

where $h_i^{\text{exc}}(\omega) = \hbar \delta(\omega - \omega_0) \delta_{i \in \text{antenna}}$ is the Fourier transform of the excitation field.

The spin current injected in the right lead can then be found from the continuity equation $\partial_t \langle S_i^z \rangle = 0$ as [17]

$$I(\omega_0) = \alpha_{\text{IF}} \int \frac{d\omega}{2\pi} \sum_{i \in \text{right lead}} \{ \omega \mathbb{G}(\omega) \mathbb{H}(\omega) \mathbb{G}^\dagger(\omega) \}_{ii}, \quad (\text{S9})$$

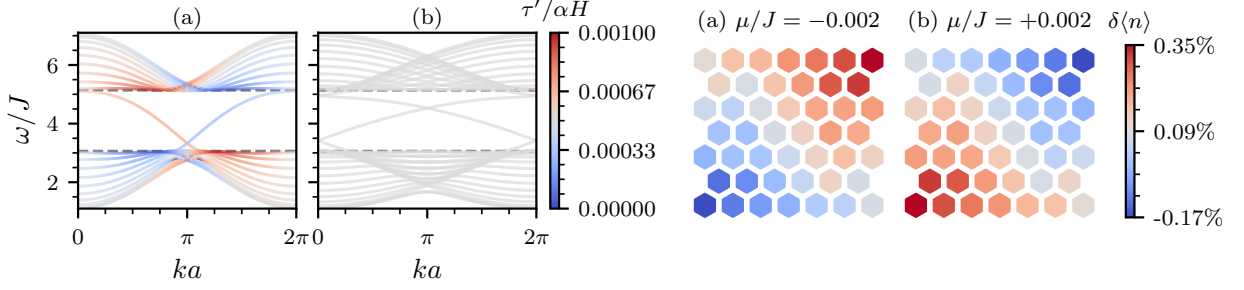


FIG. S5. (Left) The bandstructure for a zigzag (a) and armchair nanoribbon (b) with an asymmetric spin-orbit torque. The equivalent of Fig. 2 in the main text. The colorscale indicates the lifetime correction τ' induced by the spin bias $\mu/J = 1$. We still observe the same relative amplification of the left-moving edge modes compared to the right-moving modes. Note however that the lifetime correction is positive everywhere. (Right) The relative magnon density for an asymmetric spin-orbit torque, for opposite values of the spin bias μ/J : (a) -0.002 and (b) $+0.002$. The equivalent of Fig. 4 in the main text.

where $[\mathbb{H}(\omega)]_{ij} = h_i^{\text{exc}}(\omega)h_j^{\text{exc}}(\omega) = h^2\delta(\omega - \omega_0)\delta_{i \in \text{antenna}}$, the summation is over all lattice sites in contact with the right lead and α_{IF} is the interfacial Gilbert damping enhancement of the normal metal lead serving as the detector. In order to minimize reflections, we choose the Gilbert damping enhancement of the antenna and detection lead as $\alpha_{\text{IF}} = 1$.

In addition to the uniformly distributed on-site disorder δ discussed in the main text, here we also investigate the effect of defect disorder. We accounted for defect disorder by randomly removing a fraction w of the sites, implemented by setting a large on-site magnetic field $H_{\text{defect}} = 1000H$ on those sites. In addition, the spin-orbit torque is set to zero on those sites, to ensure that they are truly defects. We average over $N = 200$ realizations.

We now study the effect of disorder on the observed amplification factor $\Delta I \equiv I^{+\mu} - I^{-\mu}$, shown in Fig. S4. We first observe that in the zero disorder case, there is a strong bulk signal, comparable to the signal carried by the edge modes (top panel in Fig. S4). This signal falls off at frequencies close to the gap, for two reasons: (i) the Gilbert damping scales as ω , and thus damps higher frequency modes; (ii) the bulk modes close to the bulk band gap are dispersionless (see for example Fig. 2 in the main text), and can thus not transport angular momentum. Increasing disorder suppresses the bulk signals, whilst the edge signals remain relatively unaffected. This we therefore attribute to the topological protection of the edge states, which remains present even in the non-Hermitian phase we consider here. Note that the edge states still experience Gilbert damping, and thus have a finite lifetime.

The effect of including a disorder concentration (right panels of Fig. S4) is similar to the random on-site potential: the signal carried by the bulk modes get suppressed relative to the signal carried by the edge modes. Note that there are some slight differences in the signal as a function of frequency between the disorder concentration and the random on-site potential. Most importantly, the disorder concentration also affects the signal carried by the high-frequency edge modes, whereas the random on-site potential does not. However, the edge signal remains significantly stronger than the bulk signal, and thus we conclude that the qualitative results are independent of the chosen disorder realization.

ASYMMETRIC SPIN-ORBIT TORQUE

To contrast the scenario of sublattice-*antisymmetric* spin bias studied in the main text, we here consider the case of sublattice-*asymmetric* spin bias. Concretely, we assume that the spin accumulation is non-zero on the \mathcal{A} -sites only,

$$\mu_i = \begin{cases} \mu & i \in \mathcal{A} \\ 0 & i \in \mathcal{B} \end{cases}, \quad (\text{S10})$$

which might be experimentally more feasible, since it only requires a single normal metal layer. In what follows, we assume for simplicity that the Gilbert damping enhancement α_{sp} is still present on all sites—such that $\alpha = \alpha_0 + \alpha_{\text{sp}}$ is constant throughout the system—but this is not a necessary requirement. After linearization and Fourier transforming, we obtain the same equation of motion (4), but with $i\gamma\sigma_z \rightarrow i\gamma(\sigma_0 + \sigma_z)/2$, such that there is only an imaginary mass on the \mathcal{A} -sites. The long-wavelength excitations are then, up to first order in the dissipative terms, $\omega_{\mathbf{k}=0} = H - i(\alpha H - \gamma/2)$ and thus the system is only stable if $\gamma/2 < \alpha H$. There are therefore now two stability requirements: $\alpha_{\text{sp}}\mu/2 < \alpha H$ and $\mu < H$.

We first calculate the bandstructure for a zigzag and armchair nanoribbon, shown on the right of Fig. S5. Here we observe the same amplification of the left-moving edge modes compared to the right-moving edge modes [cf. Fig. 2 in the main text] for the

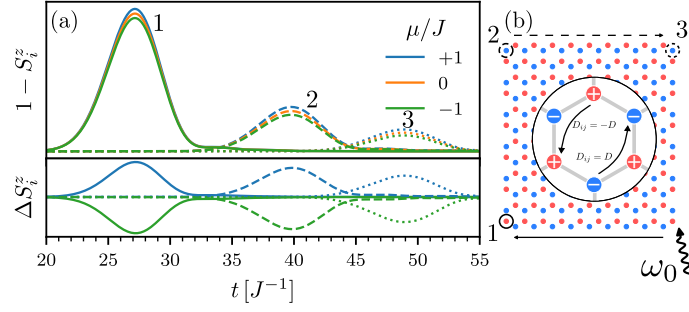


FIG. S6. (a) For an asymmetric spin-orbit torque, the spin-wave amplitude, $1 - S_i^z$ at three different sites shown, after excitation of an edge state with a pulse at frequency ω_0 at the right bottom corner, for three different values of the spin bias μ . The difference $\Delta S_z \equiv S_i^z - S_i^z|_{\mu=0}$ is shown below, i.e., the difference as the spin bias is turned on. The setup [shown in (b)] is equivalent to Fig. 1 in the main text. Note that because spin-orbit torque is only applied on one sublattice, there is no perfect cancellation of the signal at the last detector.

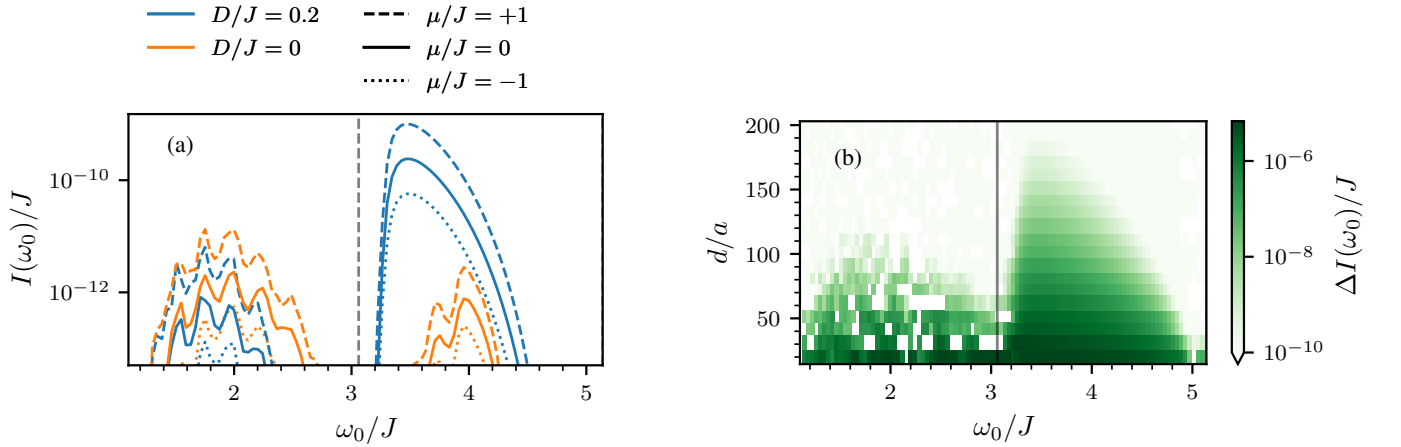


FIG. S7. The amplification for the asymmetric spin-orbit torque only applied on the \mathcal{A} -sites, with $\mu/J = 1$, i.e., Fig. 5 in the main text for asymmetric spin-orbit torque. (a) The injected spin current in the right lead, $I(\omega_0)$, as a function of excitation frequency ω_0 , at a fixed distance $d/a = 200$ comparing the topologically trivial ($D = 0$) and topologically non-trivial ($D/J = -0.2$) case and the effects of μ . (b) For $D/J = 0.2$ and $|\mu|/J = 1$, the spin current difference $\Delta I \equiv I^{+\mu} - I^{-\mu}$ between opposite signs of μ , as a function of distance, d , and excitation frequency, ω_0 .

zigzag nanoribbon. However, the lifetime correction is positive everywhere, due to the fact that $\mu_i > 0$ everywhere—as opposed to the antisymmetric setup, where μ_i has opposite signs on different sublattices. We also calculate the magnon density, as shown on the right of Fig. S5, which displays the same features as the antisymmetric setup [cf. Fig. 4 in the main text].

We next reproduce the numerical LLG simulations in Fig. S6. We observe the same amplification [cf. Fig. 1 in the main text], splitting the signal depending on the sign of the spin-orbit torque. However, because of the asymmetric nature of the spin-orbit torque, the signal is not canceled at the third detector, and is only slightly reduced.

Finally, we show the amplification of the spin current for the asymmetric setup in Fig. S7. We can clearly observe the same amplification of the topological edge states [cf. Fig. 5 in the main text]. We thus conclude that the same robust amplification of the chiral edge modes can be achieved with an asymmetric spin-orbit torque.